

Magnetic and electronic phase transitions probed by nanomechanical resonance

Makars Šiškins,^{1,*} Martin Lee,^{1,*} Samuel Mañas-Valero,² Eugenio Coronado,²
Yaroslav M. Blanter,¹ Herre S. J. van der Zant,¹ and Peter G. Steeneken^{1,3,†}

¹*Kavli Institute of Nanoscience, Delft University of Technology, Lorentzweg 1,
2628 CJ, Delft, The Netherlands*

²*Instituto de Ciencia Molecular (ICMol), Universitat de València, c/Catedrático José Beltrán 2,
46980 Paterna, Spain*

³*Department of Precision and Microsystems Engineering, Delft University of Technology, Mekelweg 2,
2628 CD, Delft, The Netherlands*

Two-dimensional (2D) materials enable new types of magnetic and electronic phases mediated by their reduced dimensionality like magic-angle induced phase transitions [1, 2], 2D Ising antiferromagnets [3] and ferromagnetism in 2D atomic layers [4, 5] and heterostructures [6]. However, only a few methods are available to study these phase transitions [3, 4, 6–8], which for example is particularly challenging for antiferromagnetic materials [6]. Here, we demonstrate that these phases can be probed by the mechanical motion: the temperature dependent resonance frequency and quality factor of multilayer 2D material membranes show clear anomalies near the phase transition temperature, which are correlated to anomalies in the specific heat of the materials. The observed coupling of mechanical degrees of freedom to magnetic and electronic order is attributed to thermodynamic relations that are not restricted to van der Waals materials. Nanomechanical resonators, therefore, offer the potential to characterize phase transitions in a wide variety of materials, including those that are antiferromagnetic, insulating or so thin that conventional bulk characterization methods become unsuitable.

A universal method to characterize phase transitions in bulk crystals is via anomalies in the specific heat, that are present at the transition temperature according to Landau’s theory [9]. However, specific heat is difficult to measure in thin micron-sized samples with a mass of less than a picogram [10, 11]. Although coupling between mechanical and electronic/magnetic degrees of freedom might not seem obvious, the intuitive picture behind this coupling is that changes in the electronic/magnetic order and entropy in a material are reflected in its specific heat, which in turn results in variations in the thermal expansion coefficient that affect the tension and resonance frequency. As the specific heat near a phase transition is expected to exhibit a discontinuity [9], the temperature dependent resonance frequency of a suspended membrane can thus be used to probe this transition. Here, we use nanomechanical motion to investigate magnetic order in membranes of semiconducting FePS₃, NiPS₃ and insulating MnPS₃ - antiferromagnetic members of the transition-metal phosphor trisulphides (MPS₃) [12], and subsequently discuss results on metallic 2H-TaS₂, which exhibits a transition to a charge density wave state [13].

FePS₃ is an Ising-type antiferromagnet with a Néel temperature in bulk in the range of $T_N \sim 118 - 123$ K [3, 12, 14], exhibiting a distinct feature in its specific heat near T_N [14]. Ionic layers in FePS₃ are stacked in van der Waals planes, that can be exfoliated to thin the crystal down with atomic precision [3]. Using mechanical exfoliation and all-dry viscoelastic stamping [15], we

transfer thin flakes of FePS₃ over circular cavities etched in an oxidised Si wafer, to form membranes (see the inset in Fig. 1a). Suspended FePS₃ devices with thicknesses ranging from 8 to 45 nm are placed in a cryostat and cooled down to a temperature of 4 K. The resonance frequency of the nanodrums is then characterized using a laser interferometry technique [16] (see Fig. 1a and Methods).

The resonance frequency of the fundamental membrane mode, $f_0(T)$, is measured in the temperature range from 4 to 200 K. Typical resonances are shown in Fig. 1b-d in the antiferromagnetic phase (80 K), near the transition (114 K) and in the paramagnetic phase (132 K), respectively. Figure 2a shows $f_0(T)$ of the same FePS₃ membrane (solid blue curve). Near the phase transition, significant changes in amplitude, resonance frequency and quality factor are observed. To analyze the data further, we first analyze the relation between f_0 and the specific heat. The decrease in resonance frequency with increasing temperature in Fig. 2a is indicative of a reduction in strain due to thermal expansion of the membrane. The observed changes can be understood by considering the resonance frequency of a bi-axially tensile strained circular membrane:

$$f_0(T) = \frac{2.4048}{\pi d} \sqrt{\frac{E}{\rho} \frac{\epsilon(T)}{(1-\nu)}}, \quad (1)$$

where E is the Young’s modulus of the material, ν its Poisson’s ratio, ρ its mass density, $\epsilon(T)$ the strain and T the temperature. The linear thermal expansion coefficient of the membrane, $\alpha_L(T)$, and silicon substrate, $\alpha_{Si}(T)$, are related to the strain in the membrane [17, 18] as $\frac{d\epsilon(T)}{dT} \approx -(\alpha_L(T) - \alpha_{Si}(T))$, using the approximation $\alpha_{SiO_2} \ll \alpha_{Si}$ (see Supplementary Section

* These authors contributed equally.

† e-mail: p.g.steeneken@tudelft.nl; h.s.j.vanderzant@tudelft.nl; m.siskins-1@tudelft.nl

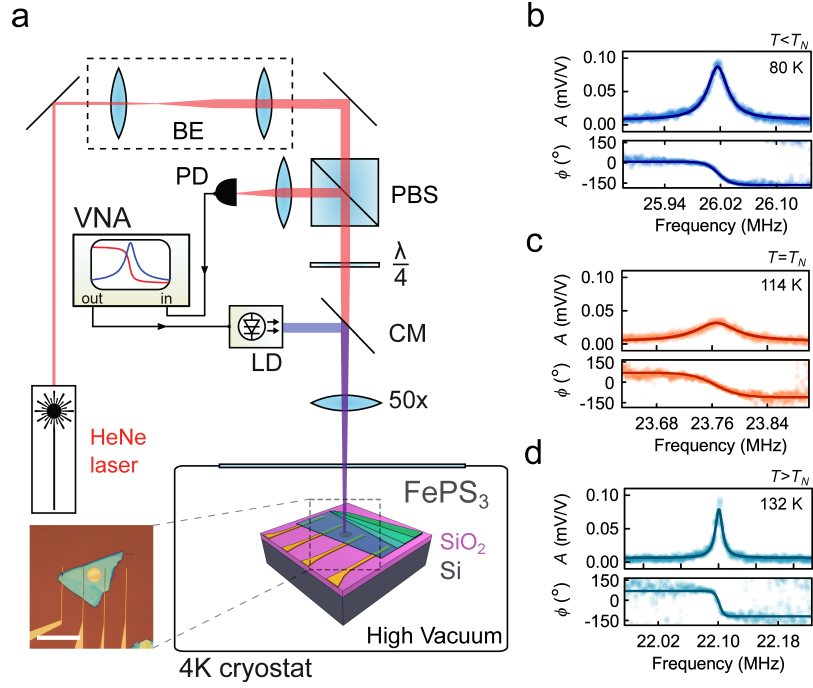


FIG. 1. Characterisation of mechanical resonances in a thin antiferromagnetic FePS₃ membrane. (a) Laser interferometry setup. Red interferometric detection laser: $\lambda_{\text{red}} = 632$ nm. Blue actuation laser diode: $\lambda_{\text{blue}} = 405$ nm. VNA - Vector Network Analyzer, CM - Cold Mirror, PBS - Polarizing Beam Splitter, PD - Photodiode, LD - Laser Diode. Inset: optical image of a FePS₃ membrane, including electrodes introducing an option for electrostatic control of strain in the membrane. Flake thickness: 45.2 ± 0.6 nm; membrane diameter: $d = 10$ μm . Scale bar: 30 μm . (b-d) Amplitude (A) and phase (ϕ) of the fundamental resonance at three different temperatures for the device shown in (a). Filled dots - measured data; solid lines - fit of the mechanical resonance used to determine f_0 and Q [16].

1). By combining the given expression for $\frac{d\epsilon(T)}{dT}$ with equation (1) and by using the thermodynamic relation $\alpha_L(T) = \gamma c_v(T)/(3KV_M)$ [19] between $\alpha_L(T)$ and the specific heat (molar heat capacity) at constant volume, $c_v(T)$, we obtain:

$$c_v(T) = 3\alpha_L(T) \frac{KV_M}{\gamma} = 3 \left(\alpha_{\text{Si}} - \frac{1}{\mu^2} \frac{d[f_0^2(T)]}{dT} \right) \frac{KV_M}{\gamma}. \quad (2)$$

Here, K is the bulk modulus, γ the Grüneisen parameter, $V_M = M/\rho$ the molar volume of the membrane and $\mu = \frac{2.4048}{\pi d} \sqrt{\frac{E}{\rho(1-\nu)}}$, that are assumed to be only weakly temperature dependent. The small effect of non-constant volume ($\nu \neq 0.5$) on c_v is neglected.

We use the equation (2) to analyze $f_0(T)$ and compare it to the calculated specific heat for FePS₃ from literature [14]. In doing so, we estimate the Grüneisen parameter following the Belomestnykh–Tesleva relation $\gamma \approx \frac{3}{2} \left(\frac{1+\nu}{2-3\nu} \right)$ [19, 20]. This is an approximation to Leont'ev's formula [21], which is a good estimation of γ for bulk isotropic crystalline solids within $\sim 10\%$ of uncertainty [19]. Furthermore, we use literature values for the elastic parameters of FePS₃ as obtained from first-principles theoretical calculations [22] to derive $E = 103$ GPa, $\nu = 0.304$ and $\rho = 3375$ kg/m³ (see Supplementary Section 2). In Fig. 2a, the steepest part of the nega-

tive slope of $f_0(T)$ (solid blue curve) leads to a large peak in $\frac{d(f_0^2(T))}{dT}$ (solid magenta curve) near 114 K, the temperature which we define as T_N and indicate by the vertical dashed lines. In Fig. 2b the specific heat curve of FePS₃ (blue solid line) as estimated from the data in Fig. 2a and equation (2) is displayed. The results are compared to a theoretical model for the specific heat of FePS₃ (magenta solid line in Fig. 2b), which is the sum of a phononic contribution from the Debye model (magenta dashed line) and a magnetic contribution as calculated by Takano, *et al.* [14]. It is noted that other, e.g. electronic contributions to $c_v(T)$ are small and can be neglected in this comparison, as is supported by experiments on the specific heat in bulk FePS₃ crystals [14]. The close correspondence in Fig. 2b between the experimental and theoretical data for $c_v(T)$ supports the applicability of equation (2). It also indicates that changes in the Young's modulus near the phase transition, that can be of the order of a couple of percent [25], are insignificant and that it is the anomaly in c_v of FePS₃ which produces the observed changes in resonance frequency and the large peak in $\frac{d(f_0^2)}{dT}$ visible in Fig. 2a.

The abrupt change in $c_v(T)$ of the membrane can be understood from Landau's theory of phase transitions [9]. To illustrate this, we consider a simplified model for an antiferromagnetic system, like FePS₃, with free energy,

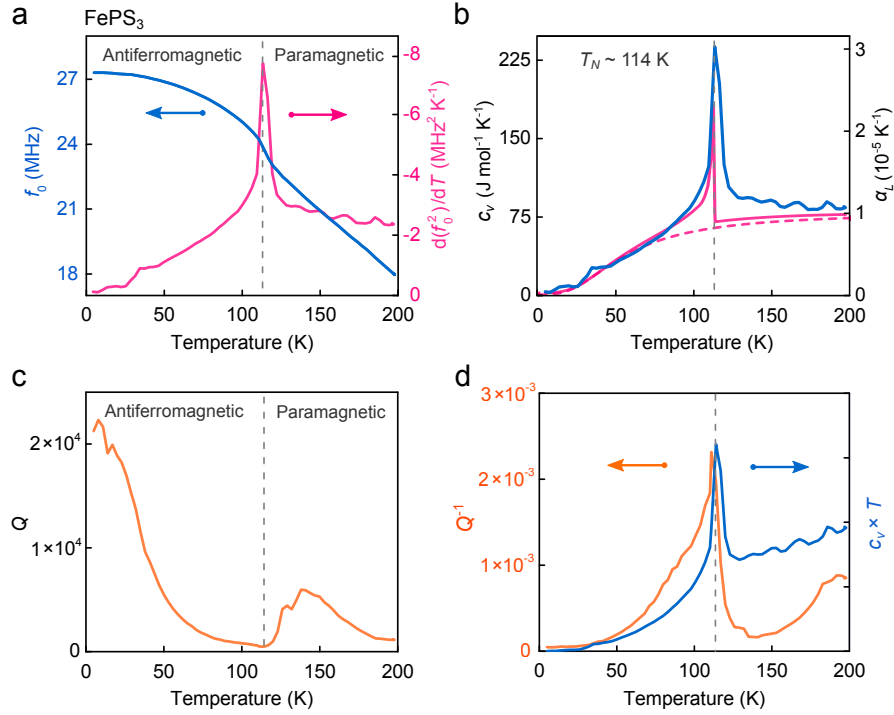


FIG. 2. Mechanical and thermal properties of a FePS₃ resonator with membrane thickness of 45.2 ± 0.6 nm. In all panels, dashed vertical lines indicate the detected transition temperature, $T_N = 114 \pm 3$ K as determined from the peak in the temperature derivative of f_0^2 . (a) Solid blue line - measured resonance frequency as a function of temperature. Solid magenta line - temperature derivative of f_0^2 . (b) Solid blue line - experimentally derived specific heat and corresponding thermal expansion coefficient. Solid magenta line - the theoretical calculation of the magnetic specific heat as reported in Takano, *et al.* [14] added to the phononic specific heat from Debye model (dashed magenta line) with a Debye temperature of $\Theta_D = 236$ K [14]. (c) Mechanical quality factor $Q(T)$ of the membrane fundamental resonance. (d) Solid orange line - measured mechanical damping $Q^{-1}(T)$ as a function temperature. Solid blue line - normalized $c_v(T) T$ term [23, 24] (see Supplementary Section 4), with $c_v(T)$ taken from (b).

F , which includes a strain-dependent magnetostriction contribution (see Supplementary Section 3). Near the transition temperature and in the absence of a magnetic field it holds that:

$$F = F_0 + [a(T - T_N) + \zeta(\epsilon)]L_z^2 + BL_z^4. \quad (3)$$

Here, a and B are phenomenological positive constants, L_z is the order parameter in the out-of-plane direction and $\zeta(\epsilon) = \eta_{ij}\epsilon_{ij}$, a strain-dependent parameter with η_{ij} a material-dependent tensor, that includes the strain and distance dependent magnetic exchange interactions between neighbouring magnetic moments. By minimizing equation (3) with respect to L_z , the equilibrium free energy, F_{min} , and order parameter are obtained (see Supplementary Section 3). Two important observations can be made. Firstly, strain shifts the transition temperature according to:

$$T_N^*(\epsilon) = T_N - \frac{\zeta(\epsilon)}{a}, \quad (4)$$

where T_N^* is the Néel temperature, below which free energy minima F_{min} with finite order ($L_z \neq 0$) appear. Secondly, since close to the transition the specific heat

follows $c_v(T) = -T \frac{\partial^2 F_{min}}{\partial T^2}$, this general model predicts a discontinuity in c_v of magnitude $T_N^* \frac{a^2}{2B}$ at the transition temperature T_N^* , in accordance with the experimental jump in $c_v(T)$ and $\frac{d(f_0^2(T))}{dT}$ observed in Fig. 2a and b.

We now analyze the quality factor data shown in Fig. 2c,d. Just above T_N , the quality factor of the resonance (Fig. 2c) shows a significant increase as the temperature is increased from 114 to 140 K. The observed minimum in the quality factor near the phase transition, suggests that dissipation in the material is linked to the thermodynamics and can be related to thermoelastic damping. We model the thermoelastic damping according to Zener [23] and Lifshitz-Roukes [24] that report dissipation of the form $Q^{-1} = \beta c_v(T) T$, where β is the thermomechanical term (see Supplementary Section 4). Since we have obtained an estimate of $c_v(T)$ from the resonance frequency analysis (Fig. 2b), we use this relation to compare the experimental dissipation $Q^{-1}(T)$ (orange solid line) to a curve proportional to $c_v(T) T$ (blue solid line) in Fig. 2d. Both the measured dissipation and the thermoelastic term display a peak near $T_N \sim 114$ K. The close qualitative correspondence between the two quantities is an indication that the thermoelastic damp-

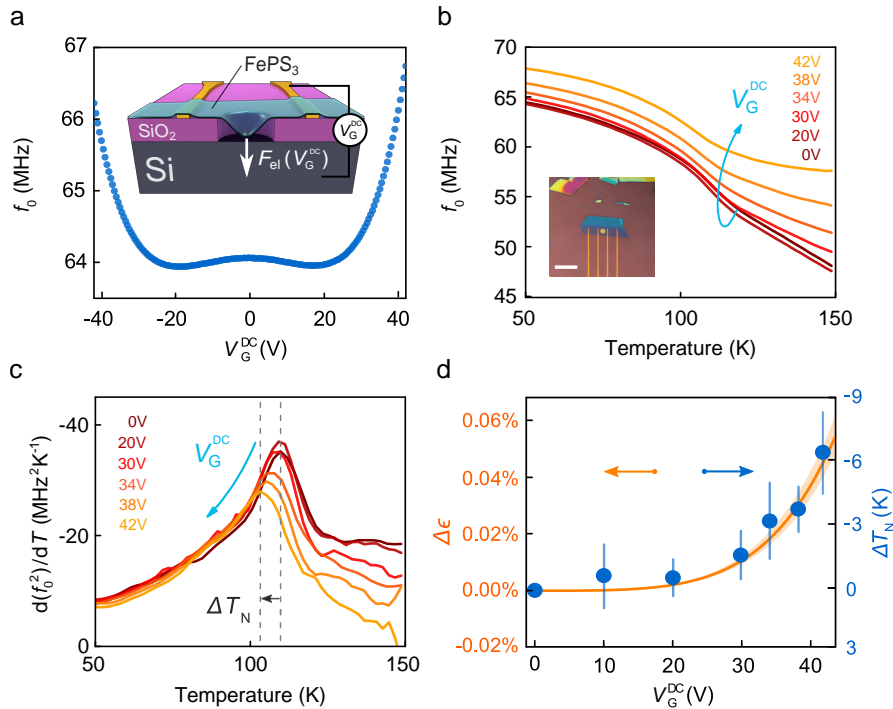


FIG. 3. Resonance frequency and transition temperature tuning with a gate voltage. (a) Resonance frequency as a function of gate voltage at 50 K. Inset - schematics of the electrostatic tuning principle. (b) Resonance frequency as a function of temperature for six different voltages. Inset: optical image of the sample, $t = 8 \pm 0.5$ nm. Scale bar: $16 \mu\text{m}$. (c) Derivative of f_0^2 as a function of gate voltage and temperature. Blue arrow, line colors and legend indicate the values of V_G^{DC} . Dashed grey lines indicate the decrease in transition temperature $\Delta T_N = T_N^*(V_G^{\text{DC}}) - T_N(0 \text{ V})$ with increasing V_G^{DC} . (d) Blue solid dots - shift in T_N as a function of V_G^{DC} . Orange solid line - model of electrostatically induced strain $\Delta\epsilon$ as a function of V_G^{DC} (see Supplementary Section 5).

ing related term indeed can account for the temperature dependence of $Q(T)$ near the phase transition. We note that the temperature dependent dissipation in thin membranes is still not well understood, and that more intricate effects might play a role in the observed temperature dependence.

Equation (4) predicts that the transition temperature is strain-dependent due to the distance dependent interaction coefficient $\zeta(\epsilon)$ between magnetic moments. To verify this effect, we use an 8 ± 0.5 nm thin sample of FePS₃ suspended over a cavity of $4 \mu\text{m}$ in diameter. A gate voltage V_G^{DC} is applied between the flake and the doped bottom Si substrate to introduce an electrostatic force that pulls the membrane down and thus strains it (see Supplementary Section 5). As shown in Fig. 3a, the resonance frequency of the membrane follows a W-shaped curve as a function of gate voltage. This is due to two counteracting effects [26]: at small gate voltages capacitive softening of the membrane occurs, while at higher voltages the membrane tension increases due to the applied electrostatic force, which causes the resonance frequency to increase.

Figure 3b shows $f_0(T)$ for six different gate voltages. The shift of the point of steepest slope of $f_0(T)$ with increasing V_G^{DC} is well visible in Fig. 3b and even more

clear in Fig. 3c, where the peak in $\frac{d(f_0^2)}{dT}$ shifts 6 K downward by electrostatic force induced strain. The observed reduction in T_N^* as determined by the peak position in $\frac{d(f_0^2)}{dT}$ qualitatively agrees with the presented model and its strain dependence from equation (4), as shown in Fig. 3d indicative of a reduced coupling of magnetic moments with increasing distance between them due to tensile strain.

Since the coupling between specific heat and the order parameter in materials is of a general thermodynamic nature, the presented methodology is applicable to a wide variety of materials provided that elastic properties of the material and Grüneisen parameter are weakly temperature dependent, the substrate satisfies the condition $\alpha_{\text{substrate}} \ll \alpha_{\text{material}}$ and that the frequency shifts and changes in Q are large enough to be resolved. We further demonstrate the method by detecting magnetic phase transitions in NiPS₃ and MnPS₃. Compared to FePS₃, the effect of the phase transitions in MnPS₃ and NiPS₃ on the resonances is more gradual (see Supplementary Section 2) with both materials showing broader maxima in $\frac{d(f_0^2(T))}{dT}$ near their T_N at 76 K and 151 K, respectively, which is consistent with measurements of bulk crystals [12, 14].

In order to demonstrate the detection of an electronic

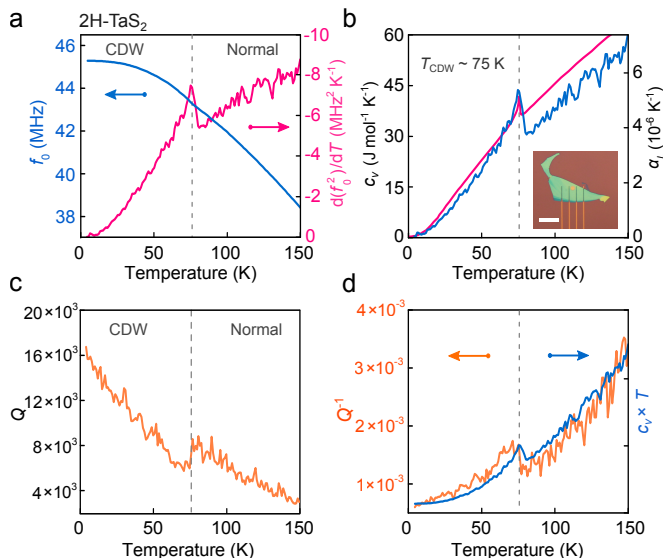


FIG. 4. Mechanical properties of a 2H-TaS₂ resonator with membrane thickness of 31.2 ± 0.6 nm and $d = 4$ μ m. Dashed vertical line in all 4 panels indicates the detected T_{CDW} , that is defined by the peak in $\frac{d(f_0^2(T))}{dT}$. (a) Solid blue line - resonance frequency as a function of temperature. Solid magenta line - temperature derivative of f_0^2 . (b) Solid blue line - experimentally derived c_v and thermal expansion coefficient as a function of temperature (see Supplementary section 6). Solid magenta line - specific heat of bulk 2H-TaS₂ as reported in Abdel-Hafez, *et al.* [13]. Inset: optical image of the sample. Scale bar: 20 μ m. (c) Quality factor $Q(T)$ as a function of temperature. (d) Solid orange line - measured mechanical damping $Q^{-1}(T)$ as a function of temperature. Solid blue line - curve proportional to the term $c_v(T)T$ [23, 24] (see Supplementary Section 4), with $c_v(T)$ taken from the experimental data in (b).

phase transition, we now discuss results for 2H-TaS₂ that in bulk exhibits a charge density wave (CDW) transition at $T_{CDW} \sim 77$ K [13]. Figure 4a shows a transition-related anomaly in both $f_0(T)$ (solid blue line) and the temperature derivative of $f_0^2(T)$ (solid magenta line) that peaks at 75 ± 3 K. We convert $\frac{d(f_0^2(T))}{dT}$ to the corresponding $c_v(T)$ using the same approach as discussed before (see Supplementary Section 6). Figure 4b shows a downward step in the specific heat at 75 K (solid blue line), indicative of a phase transition from the CDW to the disordered high-temperature state [9, 27] with a close quantitative correspondence to c_v measured in a bulk crystal [13] (drawn magenta line). This anomaly occurs near the electrically determined phase transition temperature of ~ 77 K on the same flake (see Supplementary Section 6) and is also consistent with the CDW transition temperature previously reported in 2H-TaS₂ [13]. The Q-factor also shows a local minimum with a drop next to the transition temperature (see Fig. 4c). As discussed before [23, 24], $Q^{-1}(T)$ is expected to follow the same trend as $c_v(T)T$. Both quantities are displayed in Fig. 4d and indeed show a good qualitative correspondence.

In conclusion, we have demonstrated a method for identifying phase transitions in ultrathin membranes of 2D materials via their mechanical resonance. An analytical equation for the relation between the specific heat of the material and the temperature dependent resonance frequency is derived and shown to be in good agreement with experimental results. The presented methodology thus shows that mechanical motion of suspended membranes can be used to probe magnetic and electronic order in membranes. Since the materials are characterised in a suspended state, substrate effects on the electronic and magnetic properties of the thin materials are excluded. The technique is particularly appealing for the characterisation of ultrathin membranes of antiferromagnetic and insulating materials that are difficult to characterize otherwise. It is anticipated that it can be applied to a large range of van der Waals materials [6, 8], thin 2D complex oxide sheets [28, 29] and organic antiferromagnets [30], contributing to a better understanding of fundamental models of magnetism and other ordering mechanisms in two dimensions.

METHODS

Sample fabrication To realize electrical contact to the samples for electrostatic experiments, Ti/Au electrodes are pre-patterned by a lift-off technique. Cavities are defined by reactive ion etching of circular holes with a diameter of 4–10 μ m in oxidized doped silicon wafers with an SiO₂ thickness of 285 nm. Flakes of van der Waals crystals are exfoliated from high quality synthetically grown crystals with known stoichiometry (see Supplementary Section 7). All flakes are transferred on a pre-patterned chip by an all-dry viscoelastic stamping directly after exfoliation. Subsequently, samples are kept in an oxygen free environment to avoid degradation.

Controlled measurement environment The samples are mounted on a piezo-based xy nanopositioning stage inside a chamber of a closed-cycle cryostat with optical access. A closed feedback loop controlled local sample heater is used to perform temperature sweeps at a rate of ~ 5 K/min, while keeping the pressure in the chamber below 10^{-6} mbar. During the data acquisition temperature is kept constant with ~ 10 mK stability.

Laser interferometry A blue diode laser ($\lambda = 405$ nm), which is power-modulated by a Vector Network Analyzer (VNA), is used to excite the membrane and optothermally drive it into motion. Displacements are detected by focusing a red He-Ne laser beam ($\lambda = 632$ nm) on the cavity formed by the membrane and Si substrate. The reflected light, which is modulated by the position-dependent membrane motion, is recorded by a photodiode and processed by a phase-sensitive VNA. All measurements are performed at incident laser powers of $P_{red} < 10$ μ W and $P_{blue} < 0.6$ μ W. It is checked for all membranes that the resonance frequency changes due to laser heating are insignificant. Laser spot size is on the

order of $\sim 1 \mu\text{m}$. The uncertainty in measured transition temperatures is estimated from determining the peak position in $-\frac{d(f_0^2(T))}{dT}$ within 2% accuracy in the measured maximum.

Atomic Force Microscopy AFM inspections to determine sample thickness are performed in tapping mode on a Bruker Dimension FastScan AFM. We use cantilevers with spring constants of $k = 30 - 40 \text{ N/m}$. Error bars on reported thickness values are determined by measuring three to five profile scans of the same flake.

ACKNOWLEDGMENTS

M.Š., M.L., H.S.J.v.d.Z. and P.G.S. acknowledge funding from the European Union's Horizon 2020 research and innovation program under grant agreement number 785219. H.S.J.v.d.Z., E.C. and S.M.-V. thank COST Ac-

tion MOLSPIN CA15128; E.C. and S.M.-V. thank ERC AdG Mol-2D 788222, the Spanish MINECO (Project MAT2017-89993-R co-financed by FEDER and the Unit of Excellence Maria de Maeztu MDM-2015-0538) and the Generalitat Valenciana (Prometeo Programme).

AUTHOR CONTRIBUTIONS

M.Š., M.L., E.C., H.S.J.v.d.Z. and P.G.S. conceived the experiments. M.Š. performed the laser interferometry measurements. M.L. fabricated and inspected the samples. S.M.-V. and E.C. synthesized and characterized the FePS_3 , MnPS_3 , NiPS_3 and 2H-TaS_2 crystals. M.Š., Y.M.B., and P.G.S. analysed and modeled the experimental data. H.S.J.v.d.Z. and P.G.S. supervised the project. The manuscript was jointly written by all authors with a main contribution from M.Š. All authors discussed the results and commented on the manuscript.

-
- [1] Cao, Y. *et al.* Unconventional superconductivity in magic-angle graphene superlattices. *Nature* **556**, 43–50 (2018).
- [2] Sharpe, A. L. *et al.* Emergent ferromagnetism near three-quarters filling in twisted bilayer graphene. *Science* **365**, 605–608 (2019).
- [3] Lee, J.-U. *et al.* Ising-type magnetic ordering in atomically thin FePS_3 . *Nano Lett.* **16**, 7433–7438 (2016).
- [4] Huang, B. *et al.* Layer-dependent ferromagnetism in a van der Waals crystal down to the monolayer limit. *Nature* **546**, 270–273 (2017).
- [5] Gong, C. *et al.* Discovery of intrinsic ferromagnetism in two-dimensional van der Waals crystals. *Nature* **546**, 265–269 (2017).
- [6] Gibertini, M., Koperski, M., Morpurgo, A. F. & Novoselov, K. S. Magnetic 2D materials and heterostructures. *Nat. Nanotechnol.* **14**, 408–419 (2019).
- [7] McGuire, M. A., Dixit, H., Cooper, V. R. & Sales, B. C. Coupling of crystal structure and magnetism in the layered, ferromagnetic insulator CrI_3 . *Chem. Mater.* **27**, 612–620 (2015).
- [8] Novoselov, K. S., Mishchenko, A., Carvalho, A. & Neto, A. H. C. 2D materials and van der Waals heterostructures. *Science* **353**, aac9439 (2016).
- [9] Landau, L. D., Pitaevskii, L. P. & Lifshitz, E. M. *Electrodynamics of continuous media*, vol. 8 (Butterworth, New York, 1984), 2 edn.
- [10] Morell, N. *et al.* Optomechanical measurement of thermal transport in two-dimensional MoSe_2 lattices. *Nano Lett.* **19**, 3143–3150 (2019).
- [11] Dolleman, R. J. *et al.* Transient thermal characterization of suspended monolayer MoS_2 . *Phys. Rev. Mater.* **2**, 114008 (2018).
- [12] Joy, P. A. & Vasudevan, S. Magnetism in the layered transition-metal thiophosphates MPS_3 (M=Mn, Fe, and Ni). *Phys. Rev. B* **46**, 5425–5433 (1992).
- [13] Abdel-Hafiez, M. *et al.* Enhancement of superconductivity under pressure and the magnetic phase diagram of tantalum disulfide single crystals. *Sci. Rep.* **6** (2016).
- [14] Takano, Y. *et al.* Magnetic properties and specific heat of MPS_3 (M=Mn, Fe, Zn). *J. Magn. Magn. Mat.* **272-276**, E593–E595 (2004).
- [15] Castellanos-Gomez, A. *et al.* Deterministic transfer of two-dimensional materials by all-dry viscoelastic stamping. *2D Mater.* **1**, 011002 (2014).
- [16] Castellanos-Gomez, A. *et al.* Single-layer MoS_2 mechanical resonators. *Adv. Mater.* **25**, 6719–6723 (2013).
- [17] Morell, N. *et al.* High quality factor mechanical resonators based on WSe_2 monolayers. *Nano Lett.* **16**, 5102–5108 (2016).
- [18] Singh, V. *et al.* Probing thermal expansion of graphene and modal dispersion at low-temperature using graphene nanoelectromechanical systems resonators. *Nanotechnology* **21**, 165204 (2010).
- [19] Sanditov, D. S. & Belomestnykh, V. N. Relation between the parameters of the elasticity theory and averaged bulk modulus of solids. *Tech. Phys.* **56**, 1619–1623 (2011).
- [20] Belomestnykh, V. N. & Tesleva, E. P. Interrelation between anharmonicity and lateral strain in quasi-isotropic polycrystalline solids. *Tech. Phys.* **49**, 1098–1100 (2004).
- [21] Leont'ev, K. On connection between elastic and thermal properties of substances. *Akusticheskij Zhurnal* **27**, 554–561 (1981).
- [22] Hashemi, A., Komsa, H.-P., Puska, M. & Krasheninnikov, A. V. Vibrational properties of metal phosphorus trichalcogenides from first-principles calculations. *J. Phys. Chem. C* **121**, 27207–27217 (2017).
- [23] Zener, C. Internal friction in solids I. Theory of internal friction in reeds. *Phys. Rev.* **52**, 230–235 (1937).
- [24] Lifshitz, R. & Roukes, M. L. Thermoelastic damping in micro- and nanomechanical systems. *Phys. Rev. B* **61**, 5600–5609 (2000).
- [25] Barmatz, M., Testardi, L. R. & Salvo, F. J. D. Elasticity measurements in the layered dichalcogenides TaSe_2 and NbSe_2 . *Phys. Rev. B* **12**, 4367–4376 (1975).

- [26] Lee, J. *et al.* Electrically tunable single- and few-layer MoS₂ nanoelectromechanical systems with broad dynamic range. *Sci. Adv.* **4**, eaa06653 (2018).
- [27] Saint-Paul, M. & Monceau, P. Survey of the thermodynamic properties of the charge density wave systems. *Adv. Condens. Matter Phys.* **2019**, 1–14 (2019).
- [28] Ji, D. *et al.* Freestanding crystalline oxide perovskites down to the monolayer limit. *Nature* **570**, 87–90 (2019).
- [29] Davidovikj, D. *et al.* Ultrathin complex oxide nanomechanical resonators (2019). Preprint at <https://arxiv.org/abs/1905.00056v1>.
- [30] López-Cabrelles, J. *et al.* Isorecticular two-dimensional magnetic coordination polymers prepared through pre-synthetic ligand functionalization. *Nat. Chem.* **10**, 1001–1007 (2018).

SUPPLEMENTARY INFORMATION: Magnetic and electronic phase transitions probed by nanomechanical resonance

Makars Šiškins,^{1,*} Martin Lee,^{1,*} Samuel Mañas-Valero,² Eugenio Coronado,²
Yaroslav M. Blanter,¹ Herre S. J. van der Zant,¹ and Peter G. Steeneken^{1,3,†}

¹*Kavli Institute of Nanoscience, Delft University of Technology, Lorentzweg 1,
2628 CJ, Delft, The Netherlands*

²*Instituto de Ciencia Molecular (ICMol), Universitat de València, c/Catedrático José Beltrán 2,
46980 Paterna, Spain*

³*Department of Precision and Microsystems Engineering, Delft University of Technology, Mekelweg 2,
2628 CD, Delft, The Netherlands*

CONTENTS

1. Fundamental resonance frequency of a circular plate and membrane	1
2. Mechanical resonances and specific heat of MPS ₃ (M=Fe, Ni, Mn)	2
3. Entropy in a suspended antiferromagnet	4
4. Dissipation and thermoelastic damping in vibrating membranes	5
5. Electric field induced strain in a circular FePS ₃ membrane	6
6. Mechanical resonances and specific heat of 2H-TaS ₂ near the charge density wave transition	8
7. Crystal growth and characterization	8
References	10

1. FUNDAMENTAL RESONANCE FREQUENCY OF A CIRCULAR PLATE AND MEMBRANE

In this section we analyze in more detail the resonance frequency of the FePS₃ resonators and show that near the phase transition they are close to the membrane limit. The fundamental resonance frequency of the mechanical resonator, f_0 , in the crossover membrane-plate regime can be approximated as [1, 2]:

$$f_0(T) \approx \sqrt{f_{\text{membrane}}^2 + f_{\text{plate}}^2} = \sqrt{\left(\frac{2.4048}{\pi d}\right)^2 \frac{E}{\rho} \frac{\epsilon(T)}{(1-\nu)} + \left(\frac{10.21t}{\pi d^2}\right)^2 \frac{E}{3\rho(1-\nu^2)}}, \quad (\text{S1})$$

where d is the diameter of the membrane, E the Young's modulus, $\epsilon(T)$ the strain, ν the Poisson's ratio, t the thickness, ρ the mass density and T the temperature. The resonance frequency of the fundamental mode of a circular resonator is thickness dependent. For plate resonators $f_{\text{plate}} \propto t$, as expected for small and linear deflection [1–3]. For membranes, however, f_0 is dominated by the biaxial tension N :

$$f_{\text{membrane}} = \frac{2.4048}{\pi d} \sqrt{\frac{N}{\rho t}}. \quad (\text{S2})$$

* These authors contributed equally.

† e-mail: p.g.steeneken@tudelft.nl; h.s.j.vanderzant@tudelft.nl; m.siskins-1@tudelft.nl

Equation (S2) yields $f_{\text{membrane}} \propto t^{-0.5}$ for thin resonators. When the membrane is subjected to temperature changes, the total tension is dominated by thermal strains ϵ_r^{th} . Thermal strains are of dilatational nature and do not cause any shear, thus, these can be written as: $\epsilon_r^{\text{th}} = \alpha \Delta T$, where α is the thermal expansion coefficient. In-plane radial thermal strain is then related to tension according to the Hooke's law as $N = N_0 + Et\epsilon_r^{\text{th}}/(1 - \nu)$, where N_0 the intrinsic pre-tension introduced during the fabrication process. Thus, equation (S1) is used to determine if the membranes under study are in the plate or in the membrane limit at a given temperature, as shown in Fig. S1a,b.

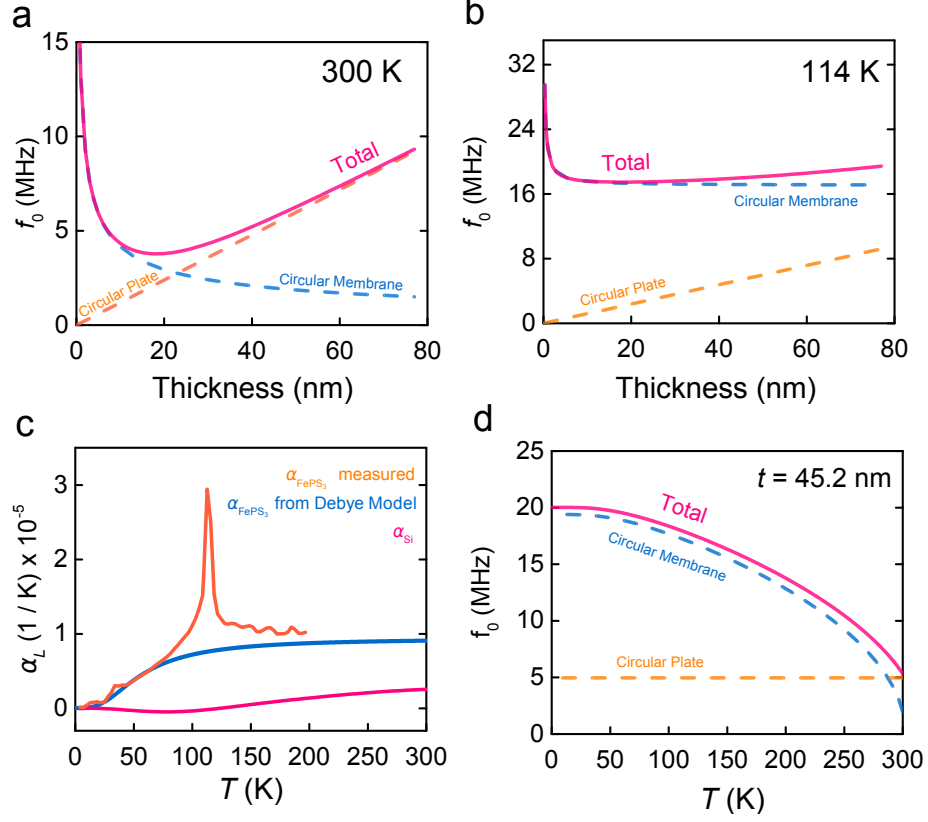


FIG. S1. Resonance frequency of a FePS₃ resonator as a function of thickness for (a) 300 K and (b) 114 K. (c) Comparison of thermal expansion coefficients of FePS₃ as measured (solid orange line) and as predicted from the Debye model (solid blue line) to that of the Si substrate (solid magenta line). (d) Calculated resonance frequency of a FePS₃ membrane using equation (S1) with a diameter of 10 μm taking into account the thermal expansion coefficient of FePS₃ as predicted by the Debye model.

The relative contribution of the plate term to the frequency of the resonator is largest at room temperature because the membrane tension is the lowest. As shown in Fig. S1a at $T = 300$ K and $N_0 = 0.1$ N/m, thicker FePS₃ samples ($t > 40$ nm) behave as circular plates. However, as shown in Fig. S1b, in proximity of the transition temperature ($T \approx 114$ K) due to temperature-induced strain $\epsilon(T)$ (see equation (S1)), the resonator behaves close to the membrane limit over a thickness range from zero to 60 nm.

The total strain in the membrane is estimated using $\epsilon(T) = \epsilon_0 - \int_{300\text{K}}^T (\alpha_{\text{material}}(T) - \alpha_{\text{Si}}(T)) dT$, where ϵ_0 is the intrinsic pre-strain at $T = 300$ K. Because $\alpha_{\text{SiO}_2} \ll \alpha_{\text{Si}}$ [4, 5], the effect of the thin SiO₂ layer can be neglected. As shown in Fig. S1c, the thermal expansion coefficient of the silicon substrate (solid magenta line) is small compared to that of FePS₃. Therefore, the total strain in the membrane will mainly build up due to α_{FePS_3} , and this term dominates the change in resonance frequency, $f_0(T)$ as depicted in Fig. S1d.

2. MECHANICAL RESONANCES AND SPECIFIC HEAT OF MPS₃ (M=Fe, Ni, Mn)

In addition to FePS₃, we measure MnPS₃ and NiPS₃ membranes with a 10 μm diameter and thicknesses of 31.8 ± 1.2 and 35.7 ± 1.1 nm, respectively. Comparative study of these is particularly interesting since FePS₃ is an Ising antiferromagnet, while the other two are Heisenberg (MnPS₃) and XY (NiPS₃) antiferromagnets. The resonance peak of the fundamental membrane mode, $f_0(T)$, as well as the Q-factor is measured from 4 – 200 K using the

procedure described in the main text.

At the phase transition, significant changes in both the resonance frequency (Fig. S2a) and quality factor (Fig. S2b) of

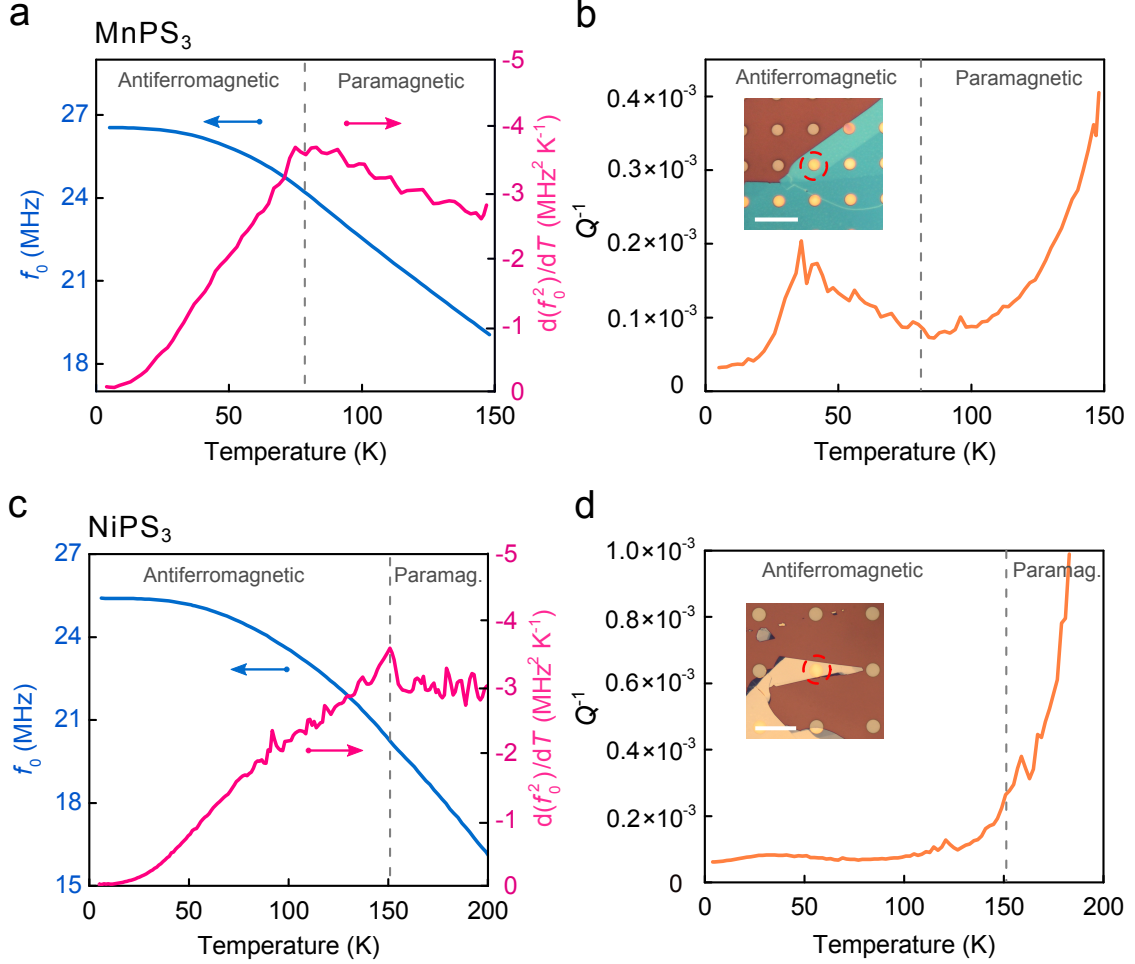


FIG. S2. Mechanical properties of MnPS₃ and NiPS₃ membranes. Dashed vertical lines indicate transition temperatures, T_N . (a) Solid blue line - Measured resonance frequency of MnPS₃ membrane as a function of temperature. Solid magenta line - Temperature derivative of f_0^2 . (b) Measured mechanical damping (Q^{-1}) as a function of temperature. Inset: Optical image of the sample, $t = 32.3 \pm 0.4$ nm. Scale bar: 40 μ m. (c) Solid blue line - Measured resonance frequency of NiPS₃ membrane as a function of temperature. Solid magenta line - Temperature derivative of f_0^2 . (d) Measured mechanical damping (Q^{-1}) as a function of temperature. Inset: Optical image of the sample, $t = 35.7 \pm 0.5$ nm. Scale bar: 30 μ m.

the MnPS₃ membrane are observed. Figure S2a shows the resonance frequency (solid blue line) and the corresponding $\frac{d(f_0^2)}{dT}$ (solid magenta line) with a peak that occurs at a temperature similar to the transition temperature from the antiferromagnetic phase (< 78 K) to the paramagnetic phase (> 78 K) in the bulk material [6] and is thus attributed as T_N . The temperature dependence of $d(f_0^2)/dT$ shows a broad hump with a smeared peak at T_N , which resembles the temperature dependent specific heat $c_v(T)$ of this material in bulk form [6]. Figure S2b shows the mechanical dissipation, Q^{-1} , that exhibits a local minimum close to T_N as well as a local maximum at $T \sim 36$ K. In Fig. S2c the resonance frequency of the NiPS₃ membrane (solid blue line) is shown with the corresponding $\frac{d(f_0^2)}{dT}$ (solid magenta line). A small peak is noticeable in $\frac{d(f_0^2)}{dT}$ near bulk $T_N \sim 155$ K indicating the phase transition [7]. However, as shown in Fig. S2d, no significant anomalies in the Q -factor were observed in the case of NiPS₃. Compared to FePS₃, the effect of the phase transitions in MnPS₃ and NiPS₃ on the resonances is more gradual (Fig. S2a-d). Both materials show a peak in $\frac{d(f_0^2)}{dT}$ at the T_N , but their dissipation does not show a clear jump at T_N like in the case of FePS₃.

We also calculated the corresponding temperature dependent specific heat $c_v(T)$ for the three MPS₃ samples. Following the methodology described in the main text, we estimate the Grüneisen parameter following the Belomestnykh–Tesleva relation [8, 9]: $\gamma \approx \frac{3}{2} \left(\frac{1+\nu}{2-3\nu} \right)$. We use reported values for monolayers of FePS₃ ($C_{11} = 72.7$

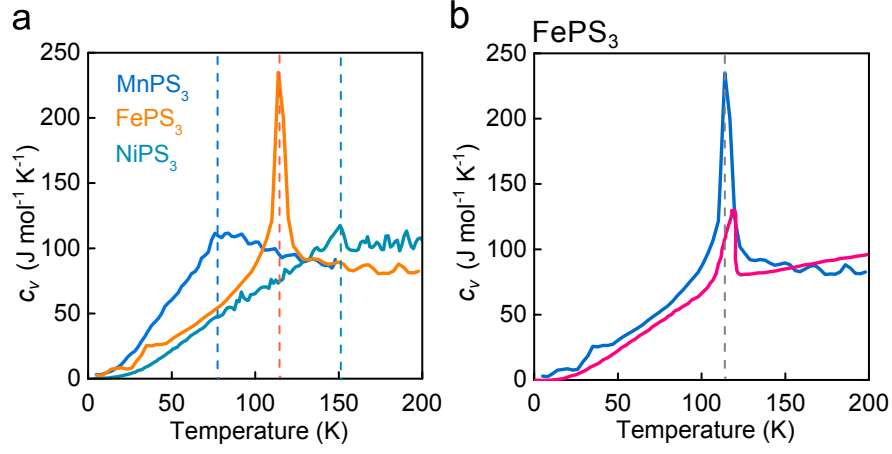


FIG. S3. Estimated specific heat (c_v) for (a) MPS_3 (M=Fe, Mn, Ni) membranes of $t = 45.2 \pm 0.6$ nm, 31.8 ± 1.2 nm and 35.7 ± 1.1 nm, respectively. Dashed lines indicate the corresponding transition temperatures (T_N): $T_N = 76 \pm 5$ K for MnPS_3 , $T_N = 114 \pm 3$ K for FePS_3 and $T_N = 151 \pm 5$ K for NiPS_3 . (b) Specific heat of ultrathin FePS_3 membrane compared to that of its bulk form. Solid blue line - measured c_v of the FePS_3 ultrathin membrane. Solid magenta line - c_v reported by Takano, *et al.* [6] for a bulk crystal.

N/m, $C_{12} = 22.1$ N/m and $\rho_{2D} = 2.16 \times 10^{-6}$ kg/m²), MnPS_3 ($C_{11} = 61.7$ N/m, $C_{12} = 20.2$ N/m and $\rho_{2D} = 2.00 \times 10^{-6}$ kg/m²) and NiPS_3 ($C_{11} = 87.0$ N/m, $C_{12} = 23.1$ N/m and $\rho_{2D} = 2.15 \times 10^{-6}$ kg/m²) as obtained from first-principles calculations [10, 11]. We convert these to three-dimensional Young's modulus E , mass density ρ and Poisson's ratio ν using $E = \frac{C_{11}^2 - C_{12}^2}{C_{11}}$, $\rho = \frac{\rho_{2D}}{t}$ and $\nu = \frac{C_{12}}{C_{11}}$, assuming the interlayer distance for the compounds to be $t_{\text{FePS}_3} = 0.64$ nm, $t_{\text{MnPS}_3} = 0.65$ nm and $t_{\text{NiPS}_3} = 0.64$ nm as determined from Fig. S7a-c. The resulting values are $E = 103$ GPa, $\nu = 0.304$ and $\rho = 3375$ kg/m³ for FePS_3 , $E = 85$ GPa, $\nu = 0.327$ and $\rho = 3076$ kg/m³ for MnPS_3 and $E = 126$ GPa, $\nu = 0.265$ and $\rho = 3359$ kg/m³ for NiPS_3 .

In Fig. S3a the specific heat for the three MPS_3 are displayed, as determined from the data in Fig. S2a,c, and Fig. 2a using equation (2) from the main text. Detected temperatures are indicated by dashed lines and found to be $T_N = 76 \pm 5$ K for MnPS_3 , $T_N = 114 \pm 3$ K for FePS_3 and $T_N = 151 \pm 5$ K for NiPS_3 , which are in agreement with experiments in bulk crystals of MPS_3 [6, 12]. As shown in Fig. S3b, for FePS_3 we obtain a good correspondence to bulk literature values [6] (solid magenta curve) without fitting parameters. The transition related peak in c_v , however, is more pronounced in the case of the ultrathin membrane (solid blue curve) than in the bulk.

3. ENTROPY IN A SUSPENDED ANTIFERROMAGNET

A uniaxial antiferromagnet with two antiparallel magnetic sub-lattices close to the phase transition can be modeled by the Landau theory of phase transitions [13, 14]. In this theory, the vector order parameter \mathbf{L} is defined as the difference between the magnetizations of the two sublattices, \mathbf{M}_1 and \mathbf{M}_2 (thus, the antiferromagnetic vector $\mathbf{L} = \mathbf{M}_1 - \mathbf{M}_2$). This order parameter is zero in the paramagnetic phase and is finite in the antiferromagnetic phase. The magnetization, \mathbf{M} , is the sum of both magnetizations ($\mathbf{M} = \mathbf{M}_1 + \mathbf{M}_2$) and equals to zero in the absence of an external magnetic field, \mathbf{H} .

For a uniaxial crystal antiferromagnet, the transition temperature is commonly known as Néel temperature, T_N , but, as conveyed by Landau, *et al.* [13, 14], it is also referred to as the antiferromagnetic Curie temperature and denoted as T_c . Note that further we will consider the Néel temperature, denoted as T_N , as the temperature where the transition from a paramagnetic to an antiferromagnetic phase takes place. Near T_N , \mathbf{L} is small and the free energy, F , can be expanded in terms of \mathbf{L} and \mathbf{H} , since the magnetization is only non-zero when an external field \mathbf{H} is present (i.e. a spin-flop transition). Following Landau formalism and considering z -axis as the main axis of symmetry, we write (see e.g. Ref. 14):

$$F = F_0 + AL^2 + BL^4 + D(\mathbf{H} \cdot \mathbf{L})^2 + D'H^2L^2 - \frac{1}{2}\chi_p H^2 + \frac{1}{2}\beta(L_x^2 + L_y^2) - \frac{1}{2}\mu_M(H_x^2 + H_y^2) - \frac{H^2}{8\pi}, \quad (\text{S3})$$

where $A = a(T - T_N)$, D , D' , a and B are phenomenological positive constants which are taken temperature independent, χ_p the isotropic susceptibility for $T > T_N$, β the index that describes the temperature dependence of

the spontaneous magnetization below T_N ($\beta > 0$ for \mathbf{L} directed out-of-plane) and μ_M the magnetic susceptibility in the paramagnetic phase. The minimization of equation (S3), where the vector \mathbf{L} is along the z -axis (thus, $L_x = L_y = 0$ and $\beta > 0$) and in the absence of field ($H = 0$), gives $L_x = L_y = 0$ and $L_z = 0$ for $T > T_N$ (paramagnetic phase) and $L_z = \sqrt{a(T_N - T)/(2B)}$ for $T < T_N$ (antiferromagnetic phase).

Now we introduce strain. For an easy-axis antiferromagnet near T_N with the vector \mathbf{L} along the z -axis and in the absence of field, we can write equation (S3) as:

$$F = F_0 + AL^2 + BL^4 + \frac{1}{2}\beta(L_x^2 + L_y^2) + \zeta L_z^2 + \zeta_x L_x^2 + \zeta_y L_y^2, \quad (\text{S4})$$

where the last three added terms describe the magnetostriction effects, i.e., the coupling of magnetic moments to strain; the coefficients ζ , $\zeta_{x,y}$ are linear combinations of the components of the strain tensor. We assume that the strain is determined by the deformation of the membrane, and that the back-action exerted by the magnetization on the strain is negligible. In that case, for the calculation of the order parameter, ζ and $\zeta_{x,y}$ can be treated as temperature-independent constants. We also assume that $|\zeta|, |\zeta_{x,y}| \ll \beta$, so that even the strained antiferromagnet exhibits an easy-axis. The minimization of equation (S4) gives $L_x = L_y = 0$, leading to a free energy which only depends on L_z ,

$$F = F_0 + [a(T - T_N) + \zeta]L_z^2 + BL_z^4. \quad (\text{S5})$$

The first observation is that the magnetostriction effects shift the antiferromagnetic phase transition point. Indeed, the phase transition occurs at the temperature T_N^* at which the coefficient multiplying L_z^2 in equation (S5) vanishes. This gives $T_N^* = T_N - \zeta/a$ (which is equation (4) in the main text).

Second, we calculate the behavior of the specific heat close to the phase transition. Minimizing equation (S5) with respect to L_z , we find the equilibrium free energy, $F_{min} = F_0 - a^2(T - T_N^*)^2/(4B)$ in the antiferromagnetic phase, where F_0 is the free energy of the paramagnetic phase. We proceed by calculating the entropy $S_{min} = -\partial F_{min}/\partial T$,

$$S_{min} - S_0 = \begin{cases} -a^2(T_N^* - T)/(2B) & T < T_N^* \\ 0 & T > T_N^* \end{cases}, \quad (\text{S6})$$

where $S_0 = -\partial F_0/\partial T$ is the entropy of the paramagnet with S_0 the non-magnetic contribution to the entropy. Since the renormalized transition temperature T_N^* is strain-dependent, the entropy of the antiferromagnet contains an additional (as compared to the paramagnetic phase) strain-dependent term. The specific heat near T_N^* , $c_{v,min} = T\partial S_{min}/\partial T$, reads

$$c_{v,min} - c_{v,0} = \begin{cases} T_N^* a^2/(2B) & T < T_N^* \\ 0 & T > T_N^* \end{cases}, \quad (\text{S7})$$

where $c_{v,0}$ is the non-magnetic contribution to the specific heat. This derivation shows, in line with Landau theory [13, 14], that the specific heat has a jump at the transition temperature, T_N^* .

4. DISSIPATION AND THERMOELASTIC DAMPING IN VIBRATING MEMBRANES

For a membrane in motion the dissipation Q^{-1} is defined as the ratio of the energy lost per cycle to 2π times the stored energy. The total dissipation in a membrane is given by the sum of all contributing dissipation mechanisms [15]:

$$Q^{-1} = Q_{medium}^{-1} + Q_{clamping}^{-1} + Q_{intrinsic}^{-1} + Q_{other}^{-1}. \quad (\text{S8})$$

Q_{medium}^{-1} is related to losses due to the interaction with a fluid medium or gas and can thus be neglected in high vacuum. $Q_{clamping}^{-1}$ is related to the transfer of mechanical energy to the anchoring substrate, which has a small temperature dependence [15]. $Q_{intrinsic}^{-1}$ quantifies all intrinsic damping mechanisms of the material, such as thermoelastic damping, internal and surface friction, and phonon-phonon interaction loss. Q_{other}^{-1} relates all other possible damping mechanisms, such as electrical charge damping and magneto-motive damping. In this section we focus on deriving the expression for the thermoelastic damping. Further derivation in this section follows Zener's standard linear solid model [16, 17].

The dissipation is equal to the ratio between the imaginary and real parts of the complex elastic modulus $E^*(\omega) = E'(\omega) + iE''(\omega)$:

$$Q^{-1} = \frac{E''}{E'}. \quad (\text{S9})$$

For a standard linear solid with a single relaxation mechanism, real and imaginary parts of the complex elastic modulus are given by:

$$E'(\omega) = E_r + (E_u - E_r) \frac{\omega^2 \tau^2}{1 + (\omega\tau)^2}, \quad E''(\omega) = (E_u - E_r) \frac{\omega\tau}{1 + (\omega\tau)^2}, \quad (\text{S10})$$

where ω is the resonance eigenfrequency, τ the thermal relaxation time, E_r and E_u are the relaxed (or isothermal) and unrelaxed (or adiabatic) Young's moduli, respectively (see Ref. 15 and 17 for more details). From equation (S9), the dissipation is then:

$$Q^{-1} = (E_u - E_r) \frac{\omega\tau}{E_r + E_u(\omega\tau)^2} \approx \frac{E_u - E_r}{E_r} \frac{\omega\tau}{1 + (\omega\tau)^2}, \quad (\text{S11})$$

for $(E_u - E_r) \ll E_r \approx E_u$. For a standard thermoelastic solid and in the case of thermoelastic damping Q_{TED}^{-1} , equation (S11) can be rewritten as [16–18]:

$$Q_{TED}^{-1} = \frac{E_u - E_r}{E_r} \beta = \frac{E\alpha^2 T}{c_v} \beta, \quad (\text{S12})$$

where α is the thermal expansion coefficient, c_v the specific heat and β the thermomechanical parameter, that in Zener's model is $\beta_Z = \frac{\omega\tau}{1 + (\omega\tau)^2}$. The exact expression for thermoelastic damping and its relation to the thermal properties of solids was found by Lifshitz and Roukes [18] with $\beta_{LR} = \frac{6}{\xi^2} - \frac{6}{\xi^3} \frac{\sinh(\xi) + \sin(\xi)}{\cosh(\xi) + \cos(\xi)}$, where $\xi = \frac{\pi}{\sqrt{2}} \sqrt{\omega\tau}$. Under the assumption that the temperature dependence of $\omega\tau$ is small, equation (S12) can be written as:

$$Q_{TED}^{-1} \propto \frac{E\alpha^2 T}{c_v}. \quad (\text{S13})$$

The close correspondence between this expression and the data in Fig. 2d and 4d in the main text indicates that this assumption is reasonable.

As could be noted from equation (2) in the main text and assuming the elastic properties of the material and its Grüneisen parameter to have a negligible temperature dependence at low temperatures, the thermoelastic damping Q_{TED}^{-1} is related to the frequency f_0 of the resonator as:

$$Q_{TED}^{-1}(T) \propto \frac{E\alpha^2(T)T}{c_v(T)} \propto c_v(T) T \propto -T \frac{d[f_0^2(T)]}{dT}, \quad (\text{S14})$$

where we use $\alpha(T) \propto c_v(T)$ and $c_v(T) \propto \frac{d[f_0^2(T)]}{dT}$ according to equation (2) in the main text. Therefore, in accordance with our observations in the main text, an anomaly (a jump) in the specific heat at the transition temperature will be visible in both $\frac{d[f_0^2(T)]}{dT}$ and $Q^{-1}(T)$ if the thermoelastic damping is the dominating dissipation mechanism.

5. ELECTRIC FIELD INDUCED STRAIN IN A CIRCULAR FePS₃ MEMBRANE

A constant electrostatic load is applied to the circular membrane with a radius a (see Fig. S4). This results in a uniform curvature R with a maximum deflection δ .

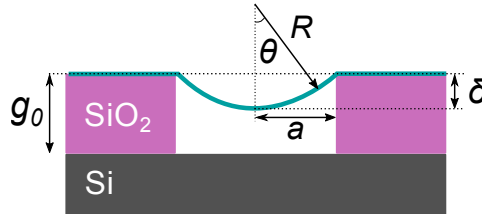


FIG. S4. Schematic of the membrane deformation, cross-section view.

In this system, the electrostatic load is balanced by the total tension N_{total} :

$$\frac{\varepsilon_0 (V_G^{\text{DC}})^2}{2(g_0 - \delta)^2} \pi R^2 = 2\pi N_{\text{total}} R, \quad (\text{S15})$$

where ε_0 is the vacuum permittivity, V_G^{DC} the applied voltage, g_0 the gap size between the membrane and the bottom silicon plate. For small deflections the radius of curvature can be approximated as:

$$R \approx \frac{a^2}{2\delta}, \quad (\text{S16})$$

so that the tension N_{total} becomes:

$$N_{\text{total}} = \frac{\varepsilon_0 (V_G^{\text{DC}})^2 a^2}{2(g_0 - \delta)^2 4\delta}. \quad (\text{S17})$$

The radial strain in such a membrane can be estimated from the arc length [19, 20]:

$$\epsilon = \frac{R\theta - a}{a} \approx \frac{a^2}{6R^2}. \quad (\text{S18})$$

Combining this result with equation (S16) yields:

$$\epsilon \approx \frac{2\delta^2}{3a^2}. \quad (\text{S19})$$

From Hooke's law and including equation (S19), one can write the strain due to deformation as:

$$N = \frac{Et}{1-\nu} \epsilon = \frac{2Et\delta^2}{3a^2(1-\nu)}, \quad (\text{S20})$$

Therefore, the total tension in the membrane, including the thermal expansion induced tension $N_0(T)$ at a certain temperature T , can be written as:

$$N_{\text{total}} = N_0(T) + N = N_0(T) + \frac{2Et\delta^2}{3a^2(1-\nu)} = \frac{\varepsilon_0 (V_G^{\text{DC}})^2 a^2}{2(g_0 - \delta)^2 4\delta}, \quad (\text{S21})$$

which also can be rewritten as:

$$V_G^{\text{DC}} = \sqrt{\frac{2(g_0 - \delta)^2}{\varepsilon_0} \left(\frac{4\delta N_0(T)}{a^2} + \frac{8Et\delta^3}{3a^4(1-\nu)} \right)}. \quad (\text{S22})$$

As shown in Fig. S5a, equation (S22) in combination with (S19) and (S1) fits the experimental data well and is used to provide an estimate of the electrostatically induced strain in the membrane (see Fig. S5b).

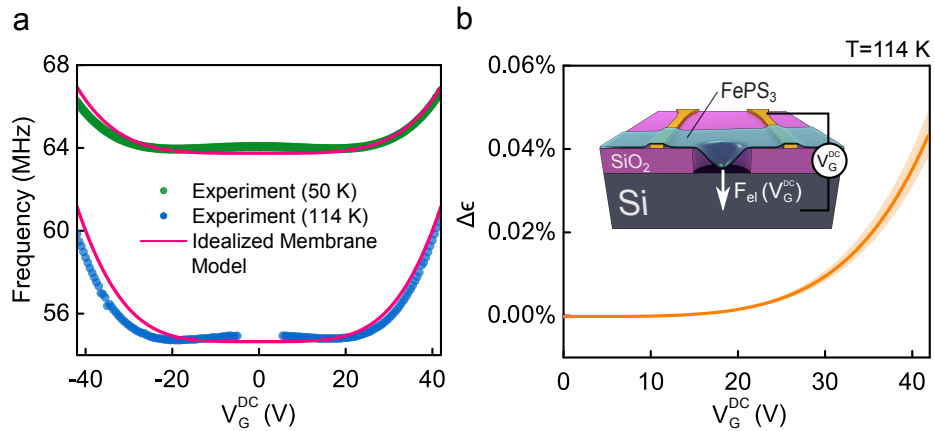


FIG. S5. (a) Idealized electrostatically strained membrane model for $N_0 = 0.01$ N/m, $g_0 = 285$ nm, $a = 2$ μ m, $t = 8$ nm, $E = 103$ GPa and $\nu = 0.304$; superimposed with corresponding experimental data. (b) Estimate of added radial strain at $T = 114$ K. The shaded orange region represents an estimated uncertainty from the accuracy in determining the temperature induced strain ($\pm 0.015\%$) at $T = 114$ K. Inset - schematics of the experiment.

6. MECHANICAL RESONANCES AND SPECIFIC HEAT OF 2H-TaS₂ NEAR THE CHARGE DENSITY WAVE TRANSITION

For 2H-TaS₂ resonance frequency measurements were performed on a $d = 4 \mu\text{m}$ drum made of a 31 nm thin flake (see Fig. S6a, solid blue line). As shown by the solid green line in Fig. S6a, the specific heat-related temperature derivative of f_0^2 reveals a clear peak at $T_{CDW} \sim 75 \text{ K}$. We convert the measured $\frac{d(f_0^2)}{dT}$ to the specific heat using the methodology described in the main text. We use reported values of $E_{2D} = 87 \text{ N/m}$ and $\nu = 0.27$ for a monolayer of 1H-TaS₂ obtained from molecular dynamics simulations [21] and mass density $\rho = 6110 \text{ kg/m}^3$. We find the corresponding $E = E_{2D}/t = 149 \text{ GPa}$, taking the interlayer spacing $t = 0.58 \text{ nm}$. The estimated specific heat of the 2H-TaS₂ membrane is depicted in Fig. S6b (solid blue line). The four-probe resistance was measured on the same flake to confirm the existence of a CDW transition using a conventional electronic based method as shown in Fig. S6c. The expected characteristic kink in the resistance is visible at $\sim 77 \text{ K}$, consistent with the CDW transition temperature previously reported in 2H-TaS₂ [22].

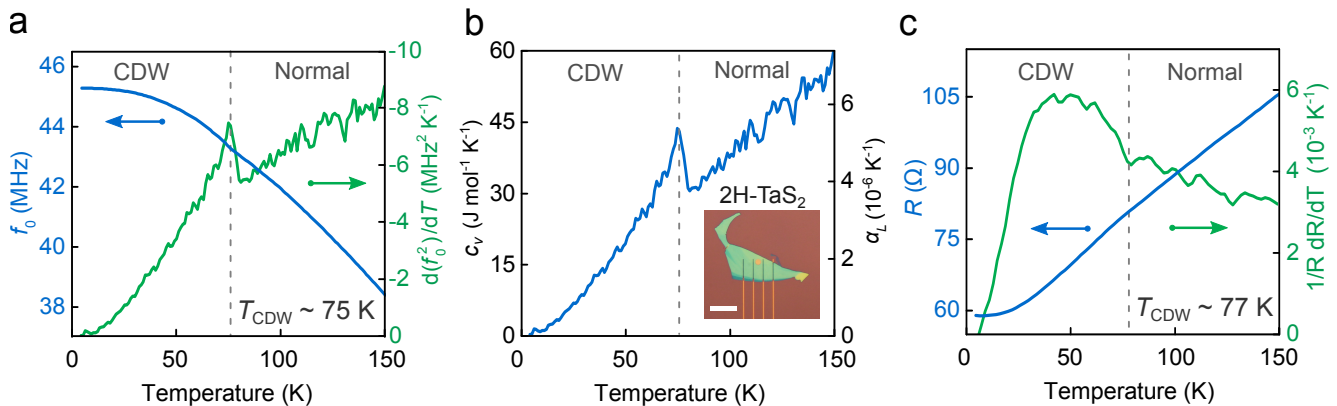


FIG. S6. Mechanical properties of a 2H-TaS₂ resonator with membrane thickness of $31.2 \pm 0.6 \text{ nm}$. Dashed vertical lines in the panels indicate the transition temperature, T_{CDW} . (a) Solid blue line - resonance frequency as a function of temperature. Solid green line - temperature derivative of f_0^2 . (b) Solid blue line - estimated specific heat (c_v) and thermal expansion coefficient (α_L). Inset: optical image of the sample. Scale bar: $20 \mu\text{m}$. (c) Solid blue line - four-point resistance of the same sample. Solid green line - $\frac{1}{R} \frac{dR}{dT}$ plot showing the CDW related feature at T_{CDW} .

7. CRYSTAL GROWTH AND CHARACTERIZATION

The crystal growth of MPS₃ (M = Mn, Fe, Ni) was performed following a typical solid state reaction. Powders of Mn (> 99.9%, from Sigma-Aldrich), Fe (99.998%, from Alfa-Aesar), Ni (99.99%, from Sigma-Aldrich), P (> 99.99%, from Sigma-Aldrich) and S (99.998%, from Sigma-Aldrich) were mixed in a stoichiometric ratio, pressed into a pellet and sealed in an evacuated quartz ampoule ($P \sim 5 \times 10^{-5} \text{ mbar}$, length = 25 cm, internal diameter = 1.5 cm) and heated from room temperature to 400 °C at 1.1 °C/min. Then, the temperature was kept constant for twenty days and slowly cooled down (0.07 °C/min).

For obtaining large crystals, 4 mmol of the previous material was mixed with I₂ as a transport agent ($[I_2] \sim 5 \text{ mg/cm}^3$) in an evacuated quartz ampoule ($P \sim 5 \times 10^{-5} \text{ mbar}$, length = 50 cm, internal diameter = 1.5 cm). The quartz tube was placed inside a three-zone furnace with the material in the leftmost zone. The other two zones were heated up in 24 h from room temperature to 650 °C and kept at that temperature for one day. After this, the leftmost side was heated up to 700 °C in 3 h and a gradient of 700 °C/650 °C/675 °C was established in the three-zone furnace. Then the temperature was kept constant for 28 days and cooled down naturally. As shown in Fig. S7, with this process we could obtain crystals with a length up to several centimeters. The obtained crystals were analyzed by ICP-OES (Inductively Coupled Plasma - Optical Emission Spectrometry) and powder X-ray diffraction. The relative weights of elements obtained are summarized in Table S7. The refinement of the X-ray diffraction pattern (Fig. S7) revealed a monoclinic base-centered crystal system with C12/m1 space group and a unit cell determined by $\alpha = \gamma = 90^\circ$ and $\beta = 107.33(1)^\circ$ (MnPS₃), $\beta = 107.13(1)^\circ$ (FePS₃), $\beta = 106.945(9)^\circ$ (NiPS₃), and $a = 6.077(7) \text{ \AA}$, $b = 10.55(2) \text{ \AA}$ and $c = 6.805(9) \text{ \AA}$ for MnPS₃, $a = 5.939(6) \text{ \AA}$, $b = 10.296(3) \text{ \AA}$ and $c = 6.716(3) \text{ \AA}$ for FePS₃ and $a = 5.815(4) \text{ \AA}$, $b = 10.087(5) \text{ \AA}$ and $c = 6.627(4) \text{ \AA}$ for NiPS₃. The obtained results are in accordance with the ones reported in the literature [23].

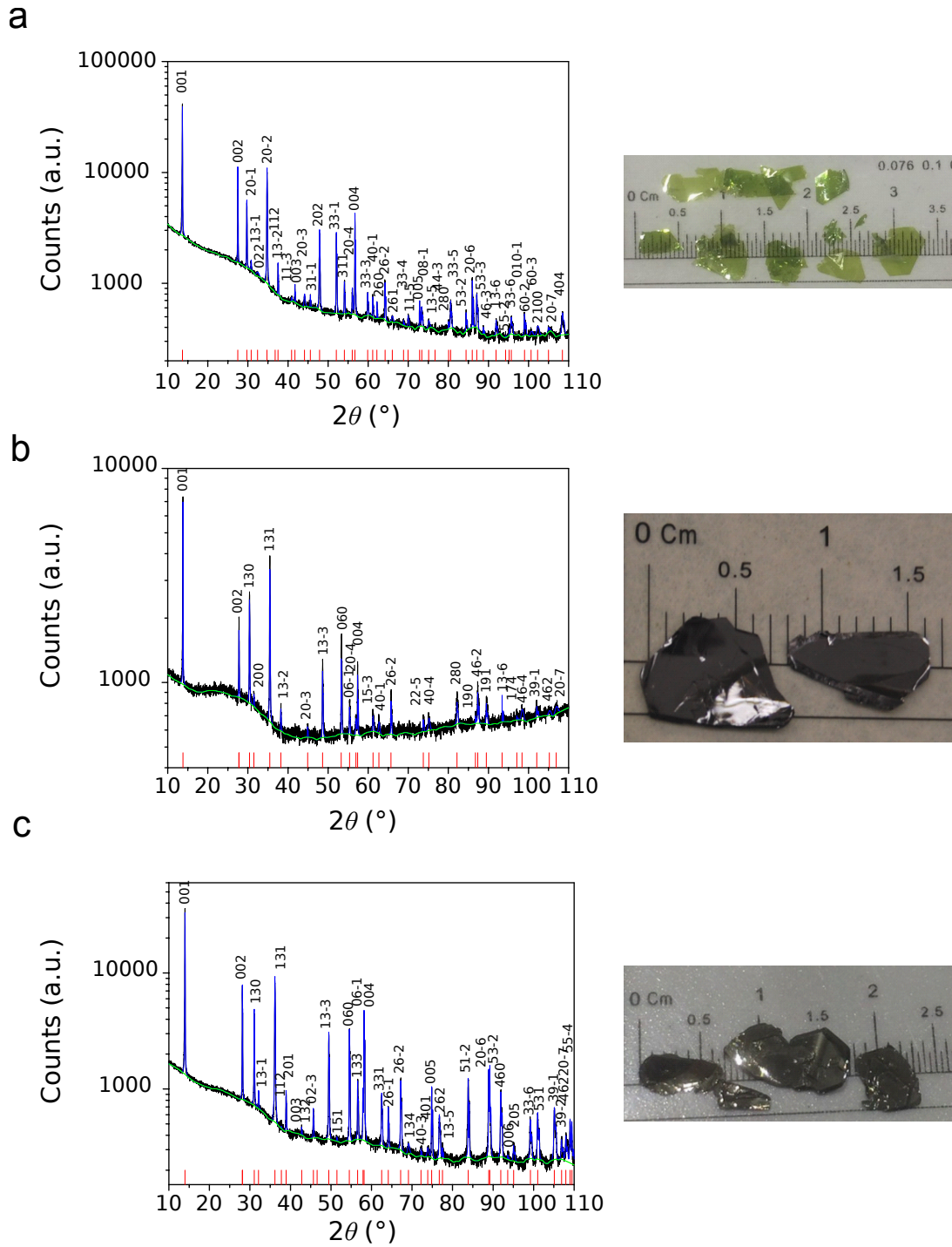


FIG. S7. XRPD experimental patterns (black) and corresponding fits (peaks in blue and background in green) for MPS_3 ($M = \text{Mn, Fe and Ni}$) crystals. For clarity, the peaks have been marked by red lines. (a) Left: Pattern of MnPS_3 . Right: Photography of a MnPS_3 crystal. The fit gives as a result: $a = 6.077(7)$ Å, $b = 10.55(2)$ Å and $c = 6.805(9)$ Å, $\alpha = \gamma = 90^\circ$ and $\beta = 107.33(1)^\circ$, monoclinic C face center crystal system with $C12/m1$ space group, $\chi^2 = 5.8 \times 10^{-5}$. (b) Left: Pattern of FePS_3 . Right: Photography of a FePS_3 crystal. The fit gives as a result: $a = 5.939(6)$ Å, $b = 10.296(3)$ Å and $c = 6.716(3)$ Å, $\alpha = \gamma = 90^\circ$ and $\beta = 107.13(1)^\circ$, monoclinic C face center crystal system with $C12/m1$ space group, $\chi^2 = 1.5 \times 10^{-6}$. (c) Left: Pattern of NiPS_3 . Right: Photography of a NiPS_3 crystal. The fit gives as a result: $a = 5.815(4)$ Å, $b = 10.087(5)$ Å and $c = 6.627(4)$ Å, $\alpha = \gamma = 90^\circ$ and $\beta = 106.945(9)^\circ$, monoclinic C face center crystal system with $C12/m1$ space group, $\chi^2 = 1.1 \times 10^{-5}$.

The crystal growth and characterization of 2H-TaS₂ was performed as already reported in earlier works [24, 25].

Element		Obtained (%)	Expected (%)
MnPS ₃	Mn	28.0 ± 1.0	30.2
	P	12 ± 1	17.0
	S	49 ± 2	52.8
FePS ₃	Fe	30.0 ± 1.0	30.5
	P	15.7 ± 0.5	16.9
	S	51 ± 2	52.6
NiPS ₃	Ni	30.0 ± 1.0	31.6
	P	15.7 ± 0.5	16.6
	S	53 ± 2	51.8

TABLE SI. Experimental and expected relative weights analyzed by inductively coupled plasma - optical emission spectrometry (ICP-OES) for the different MPS₃ crystals (M = Mn, Fe and Ni).

-
- [1] Wah, T. Vibration of circular plates. *J. Acoust. Soc. Am.* **34**, 275–281 (1962).
- [2] Castellanos-Gomez, A. *et al.* Single-layer MoS₂ mechanical resonators. *Adv. Mater.* **25**, 6719–6723 (2013).
- [3] Timoshenko, S., Young, D. H. & Weaver, W. *Vibration Problems in Engineering* (Wiley, New York, 1974), 4 edn.
- [4] White, G., Birch, J. & Manghnani, M. H. Thermal properties of sodium silicate glasses at low temperatures. *J. Non-Cryst. Solids* **23**, 99–110 (1977).
- [5] Lyon, K. G., Salinger, G. L., Swenson, C. A. & White, G. K. Linear thermal expansion measurements on silicon from 6 to 340 K. *J. Appl. Phys.* **48**, 865–868 (1977).
- [6] Takano, Y. *et al.* Magnetic properties and specific heat of MPS₃ (M=Mn, Fe, Zn). *J. Magn. Magn. Mater.* **272-276**, E593–E595 (2004).
- [7] Kim, K. *et al.* Suppression of magnetic ordering in XXZ-type antiferromagnetic monolayer NiPS₃. *Nat. Commun.* **10** (2019).
- [8] Sanditov, D. S., Mashanov, A. A., Darmaev, M. V., Sanditov, B. D. & Mantatov, V. V. Grüneisen parameter and elastic constants of crystals and vitreous bodies. *Russ. Phys. J.* **52**, 221–230 (2009).
- [9] Belomestnykh, V. N. & Tesleva, E. P. Interrelation between anharmonicity and lateral strain in quasi-isotropic polycrystalline solids. *Tech. Phys.* **49**, 1098–1100 (2004).
- [10] Hashemi, A., Komsa, H.-P., Puska, M. & Krasheninnikov, A. V. Vibrational properties of metal phosphorus trichalcogenides from first-principles calculations. *J. Phys. Chem. C* **121**, 27207–27217 (2017).
- [11] Zhang, X., Zhao, X., Wu, D., Jing, Y. & Zhou, Z. MnPSe₃ monolayer: A promising 2D visible-light photohydrolytic catalyst with high carrier mobility. *Adv. Sci.* **3**, 1600062 (2016).
- [12] Joy, P. A. & Vasudevan, S. Magnetism in the layered transition-metal thiophosphates MPS₃ (M=Mn, Fe, and Ni). *Phys. Rev. B* **46**, 5425–5433 (1992).
- [13] Landau, L. D. On the theory of phase transitions. *Zh. Eksp. Teor. Fiz.* **7**, 19–32 (1937). [*Ukr. J. Phys.* **53**, 25 (2008)].
- [14] Landau, L. D., Pitaevskii, L. P. & Lifshitz, E. M. *Electrodynamics of continuous media*, vol. 8 (Butterworth, New York, 1984), 2 edn.
- [15] Schmid, S., Villanueva, L. G. & Roukes, M. L. *Fundamentals of Nanomechanical Resonators* (Springer International Publishing, 2016).
- [16] Zener, C. Internal friction in solids. I. Theory of internal friction in reeds. *Phys. Rev.* **52**, 230–235 (1937).
- [17] Zener, C. Internal friction in solids II. General theory of thermoelastic internal friction. *Phys. Rev.* **53**, 90–99 (1938).
- [18] Lifshitz, R. & Roukes, M. L. Thermoelastic damping in micro- and nanomechanical systems. *Phys. Rev. B* **61**, 5600–5609 (2000).
- [19] Small, M. K. & Nix, W. Analysis of the accuracy of the bulge test in determining the mechanical properties of thin films. *J. Mater. Res. Technol.* **7**, 1553–1563 (1992).
- [20] Weber, P., Güttinger, J., Tsioutsios, I., Chang, D. E. & Bachtold, A. Coupling graphene mechanical resonators to superconducting microwave cavities. *Nano Lett.* **14**, 2854–2860 (2014).
- [21] Jiang, J.-W. & Zhou, Y.-P. Parameterization of Stillinginger-Weber potential for two-dimensional atomic crystals. In *Handbook of Stillinginger-Weber Potential Parameters for Two-Dimensional Atomic Crystals* (IntechOpen, 2017).
- [22] Abdel-Hafez, M. *et al.* Enhancement of superconductivity under pressure and the magnetic phase diagram of tantalum disulfide single crystals. *Sci. Rep.* **6** (2016).
- [23] Ouvrard, G., Brec, R. & Rouxel, J. Structural determination of some MPS₃ layered phases (M = Mn, Fe, Co, Ni and Cd). *Mater. Res. Bull.* **20**, 1181–1189 (1985).
- [24] Pinilla-Cienfuegos, E. *et al.* Local oxidation nanolithography on metallic transition metal dichalcogenides surfaces. *Appl. Sci.* **6**, 250 (2016).

[25] Navarro-Moratalla, E. *et al.* Enhanced superconductivity in atomically thin TaS₂. *Nat. Commun.* **7** (2016).